

# Observation of Radiation Pressure Shot Noise

T. P. Purdy\*, R. W. Peterson, and C. A. Regal

September 28, 2012

JILA, University of Colorado and National Institute of Standards and Technology,  
and Department of Physics, University of Colorado, Boulder, Colorado 80309, USA

\* To whom correspondence should be addressed; Email: tpp@jila.colorado.edu

## Abstract

The quantum mechanics of position measurement of a macroscopic object is typically inaccessible due to strong environmental coupling and classical noise. Here we show that a micromechanical membrane resonator subject to an increasingly strong continuous position measurement exhibits a quantum mechanical back action force that rises in accordance with the Heisenberg uncertainty relation. For our optically-based position measurements, the specific form of the back action is that of a fluctuating radiation pressure from the Poisson-distributed photons in the coherent measurement field, termed radiation pressure shot noise. We demonstrate a radiation pressure shot noise drive that is comparable in magnitude to the thermal forces in our system. Additionally, we observe a temporal correlation between the fluctuations in radiation force and position of the resonator that may also be interpreted as a quantum non-demolition measurement of the photon field.

It is a well-known principle of quantum mechanics that any position measurement must be accompanied by a back action force that perturbs the momentum of the system. For an optically-based ideal position measurement, the manifestation of this back action force is termed radiation pressure shot noise (RPSN) [1, 2, 3]. Here, for example, the Poisson distributed photons (shot noise) of a coherent optical field reflect off the object to be measured, transferring recoil momentum at random times. For a harmonically bound object measured over many oscillation periods and by the accumulation of many photons, the increased spread in momentum will lead to a corresponding increase in displacement fluctuations, obscuring the initial position. Additionally, shot noise directly sets an imprecision noise floor on any method of optical detection. The point in an ideal measurement where the imprecision from the sum of these two effects is minimized is termed the standard quantum limit (SQL) [3, 4, 5, 6].

This idealized picture of quantum measurement and back action for large objects is typically obscured by classical noise sources such as thermal motion. Indeed, no solid object has yet been put into the regime where RPSN is the dominant driving force. The back action effect of RPSN is more readily observed if the measurement strength is increased beyond the SQL. As illustrated in Fig. 1A, the level of back action increases linearly with optical power or measurement strength. Radiation pressure effects are expected to soon limit precision interferometric measurements such as the LIGO gravitational wave detector. In the next generation of LIGO, extremely high laser powers will enhance strain sensitivity at high frequencies; with such powers RPSN is predicted to dominate the sensitivity at intermediate frequencies, even with large test masses at room temperature [2, 7]. Such quantum limits to continuous position measurement have long been

foreseen, and many ideas have been developed to circumvent the SQL by employing quadrature-squeezed light [8] or back action evasion techniques [9].

While a shot noise imprecision noise floor is a ubiquitous measurement limitation, the experimental signatures of RPSN have remained elusive. Effects of RPSN have been observed in samples of dilute, laser cooled atomic gas [10, 11], and several groups have made both experimental and theoretical studies of the predicted signatures of RPSN [12, 4, 13, 14, 15, 16]. A new promising direction is low-mass, high-frequency, and high-optomechanical-coupling mechanical resonators that have been developed in the context of cavity optomechanics. Their enhanced response to optical forces makes them an ideal platform to study the effects of RPSN. In such devices analogous effects of electron shot noise measurement back action have been observed [17]. Also, measurements of a weakly optically probed nanomechanical resonator have been interpreted as arising from correlations between sensing noise and back action [18]. Some of these nanomechanical resonators have even recently been cooled with electromagnetic radiation to near their quantum mechanical ground state [19, 20, 21], illustrating the capacity for dominant coherent optical forces. In this report, we demonstrate a micro-optomechanical resonator where the effects of RPSN are comparable in magnitude to those of the thermal forces. We observe the increased average amplitude of motion expected from RPSN; we also demonstrate temporal correlations between the optical driving force and the resonator position that can be interpreted as a quantum non-demolition (QND) measurement of intracavity photon fluctuations using the mechanical object as a meter.

Our optomechanical system consists of a silicon nitride membrane microresonator [22, 23] inside of a Fabry-Perot optical cavity specially designed to operate at cryogenic temperatures (See Fig. 2 and Ref. [24]). Pioneering work by a group at Yale [22], has shown that such systems can achieve both large optomechanical coupling and very weak environmental coupling through optical and mechanical loss channels. Optomechanical coupling is achieved through a dispersive interaction, where the cavity resonance frequency shifts with the location of membrane along the optical standing wave. This interaction imprints phase and amplitude modulation on laser light transmitted through the system, which allows for measurement of the membrane motion. In conjunction, the laser applies an optical gradient force to the membrane, pushing it toward higher optical intensity. The mechanical modes are those of a highly tensioned square plate 0.5 mm on a side and 40 nm thick, with an effective mass of about 7 ng. We operate in a helium flow cryostat at a temperature of 4.9 K, where intrinsic mechanical linewidths,  $\Gamma_0/2\pi$ , are typically less than 1 Hz. For the (2,2) mode oscillating at  $\omega_m/2\pi = 1.55$  MHz (twice the fundamental mode frequency), we achieve a maximum single photon coupling rate  $g/2\pi = 17$  Hz.

We use two laser fields in the cavity, derived from the same 1064 nm laser source, both coupled to the same spatial mode of the cavity, but with orthogonal polarizations [12, 13]. All other optical modes are far enough separated in frequency to be neglected. The half-planar, 5.1 mm length,  $72\ \mu\text{m}$  mode waist cavity typically has a full linewidth  $\kappa/2\pi \sim 1$  MHz, which varies slightly with the membrane position. The “signal” beam, typically of much larger intensity than the other, is maintained on the optical resonance via active feedback. This beam provides the RPSN. Its transmitted shot noise intensity fluctuations constitute a record of the optical force on the resonator. The corresponding sensitive position measurement is wholly imprinted in the unrecorded phase modulation spectrum. Additional phase noise from fluctuations in the cavity-laser detuning would preclude fully shot-noise-limited phase-quadrature detection in this system [24]. The much weaker “meter” beam is tuned to the red of the optical resonance. The resonator’s displacement spectrum is imprinted in the transmitted intensity spectrum of this laser. While its shot noise drive is much smaller, the meter beam provides optical Raman sideband cooling of the mechanical resonator [25]. The optical damping greatly eases the requirements on the relative detuning of the signal beam from the cavity resonance due to both the onset of parametric instabilities at positive detuning and the contamination of cross correlation measurements by thermal motion near the mechanical resonance [14, 16]. However, Raman cooling does not

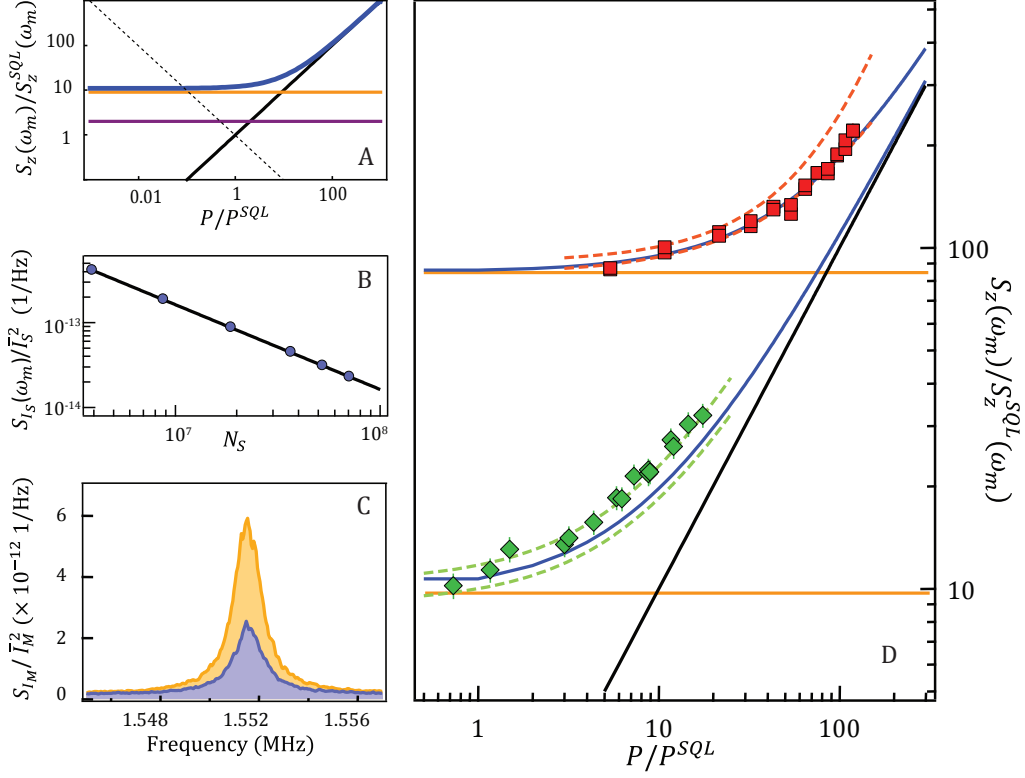


Figure 1: Displacement spectrum measurements. (A) Canonical picture of continuous position measurement. Contributions are: RPSN (black), thermal motion (orange), and zero point motion (purple). They combine to give the expected result of our measurement (blue). The dashed curve represents the effective displacement noise from the shot noise limited imprecision of an ideal measurement. (B) Spectral density for signal beam photocurrent near  $\omega_m$  (blue circles) for device A and measured shot noise floor (black). (C) Transmission spectra for device B at  $N_S = 2.0 \times 10^7$  (blue) and  $N_S = 3.6 \times 10^8$  (orange). (D) Plotted versus signal power  $P$  are: Peak displacement spectral density for device A (green diamonds) and device B (red squares), expected values (blue), thermal contribution (orange), bounds on theoretical estimates including systematic uncertainty in device parameters and classical noise contribution (dashed), and expected RPSN contribution (black). Parameters for Device A (Device B):  $g/2\pi = 16.3 \pm 0.6$  Hz ( $16.1 \pm 0.3$  Hz),  $\kappa/2\pi = 1.17$  MHz ( $0.89$  MHz),  $\Delta_S/2\pi = 1.5 \pm 1.5$  kHz ( $2 \pm 0.5$  kHz),  $\Delta_M/2\pi = 1.6$  MHz ( $0.7$  MHz),  $N_M = 3.4 \pm 0.3 \times 10^6$  ( $7.0 \pm 0.3 \times 10^6$ ),  $N_S^{\max} = 1.2 \pm 0.1 \times 10^8$  ( $4.4 \pm 0.1 \times 10^8$ ),  $\omega_m/2\pi = 1.575$  MHz ( $1.551$  MHz),  $\Gamma_0/2\pi = 0.116$  Hz ( $0.47$  Hz),  $\Gamma_m/2\pi = 3$  kHz ( $1.43$  kHz).

increase the ratio of peak displacement due to RPSN versus the thermal displacement, as the resonator's response to both forces is damped equally in the cooling process.

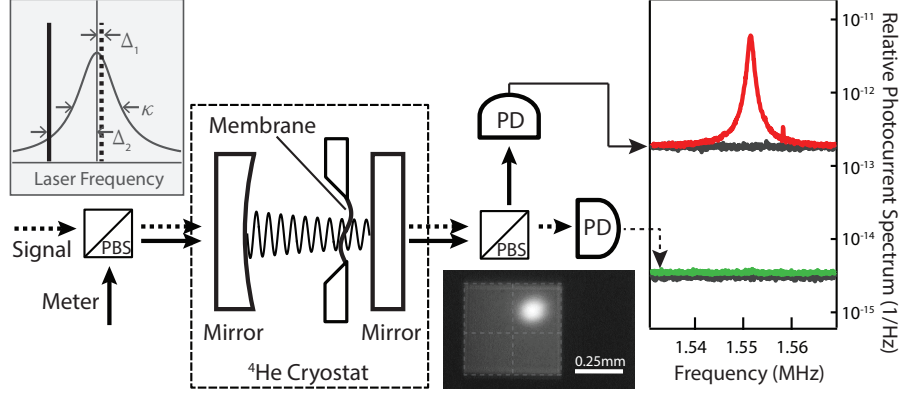


Figure 2: Experimental Setup. The signal and meter beams are combined and separated with polarizing beam splitters (PBS) before and after interacting with the optomechanical cavity, and detected directly on photodetectors (PD). The inset photograph shows an in-situ image of the square membrane and optical mode spot, with dashed lines indicating the nodes of (2,2) mechanical mode. The plot on the right shows spectra from device B of the photocurrents  $S_{I_S}(\omega)/\bar{I}_S^2$  (green),  $S_{I_M}(\omega)/\bar{I}_M^2$  (red), as well as the noise floors that include detector noise and the dominant shot noise (gray).

The effect of the optomechanical coupling on the resonator from a single laser [25, 26], or multiple beams in orthogonal modes [14] has been well studied. The resonator's mechanical susceptibility is modified to include optomechanical damping and frequency shifts from each laser. Additionally, the amplitude of motion, or effective phonon occupation is modified. The optomechanical damping cools the resonator, while RPSN increases the amplitude of motion. In equilibrium, an effective phonon occupation can be computed from a simple rate equation as  $n_m = (n_{th}\Gamma_0 + n_S\Gamma_S + n_M\Gamma_M)/\Gamma_m$ . Here  $n_{th}$  is the thermal phonon occupation;  $n_S$  and  $\Gamma_S$  ( $n_M$  and  $\Gamma_M$ ) are the effective bath temperature and optomechanical damping rate of the signal (meter) laser. The total mechanical damping rate is  $\Gamma_m = \Gamma_0 + \Gamma_S + \Gamma_M$ . In our experiments  $\Gamma_M \gg \Gamma_0$ ,  $\Gamma_S$ , while  $\Delta_S \sim 0$  and  $N_S \gg N_M$ , where  $\Delta_S$ ,  $N_S$  ( $\Delta_M$ ,  $N_M$ ) are the detuning from cavity resonance and intracavity photon occupation of the signal (meter) beam. The RPSN dominates over thermal noise when  $R_S = C_S/n_{th}(1 + (2\omega_m/\kappa)^2)^{-1} > 1$ , where  $C_S = 4N_S g^2/\kappa\Gamma_0$  is the multiphoton cooperativity. We are able to reach this high cooperativity regime due to the small mass, weak intrinsic damping, and cryogenic environment of our resonator.

The increase in phonon occupation due to RPSN is shown in Fig. 1. Transmission spectra,  $S_{I_M}(\omega)$ , for the meter beam are shown in Fig. 1B for the case of negligible  $N_S$  and for  $N_S$  sufficiently large that  $R_S \sim 1$ . We observe a marked increase in the spectral area and hence  $n_m$ . Fig. 1D shows, for two different devices, A and B, the peak displacement spectral density,  $S_z(\omega_m)$ , inferred from transmitted intensity spectra. The parameters of each device are similar, except  $\Gamma_0$  is much smaller for device A, while device B has a much lower optical loss. Thus, device A enters the RPSN dominated regime at lower  $N_S$  than device B, while device B provides higher signal-to-noise measurements. We scale the peak displacement spectral density by the SQL peak spectral density  $S_z^{SQL}(\omega_m) = \hbar/m\omega_m\Gamma_m$  [5], at the damping provided by the meter beam used in the measurement. The optical measurement strength is scaled such that  $P/P^{SQL} = 1$  at the SQL. Working in these quantum measurement units allows for direct comparison of the two devices. The increased spectral

density also includes a small contribution from classical radiation pressure noise. The total transmitted noise spectral density of the signal beam is shown in Fig 1C. For device A, at all measured laser powers, the noise level is within a few percent of the measured shot noise level at the photodetector. This noise level, referred back to the intracavity level, puts an upper bound of at most 15% of the displacement signal arising from classical laser noise. Taking into account the thermal motion and classical intensity noise, we can attribute at least 55% of the total displacement spectrum to RPSN for device A at the maximum signal beam strength. For device B this lower bound is 40%. The dashed curves of Fig. 1D represent bounds on the expected spectral densities accounting for systematic uncertainties in the device parameters including uncertainty in the classical noise level. Another effect that might mimic the effect of RPSN is physical heating. To test for physical heating, we monitor the response of a higher frequency, weakly optomechanically coupled mechanical mode where RPSN effects are expected to be negligible. This response indicates the bath temperature for the higher-frequency mode, and hence for our mode of interest if we assume a common thermal bath, does not rise by more than 10% due to absorbed laser light. Details of the calibration process are given in the Supplemental Material.

We now turn to the study of the temporal correlations between the signal beam photocurrent, which records the radiation pressure drive, and the meter beam photocurrent, which contains the mechanical response to the RPSN. We compute the spectrum of the two-time cross correlation function  $S_{ISM}(\omega) = \langle I_S^*(\omega) I_M(\omega) \rangle$ , where  $I(\omega)$  is the complex Fourier transformation of the photocurrent  $I(t)$ , and the angle brackets represent an average over many realizations of the experiment. In the limit  $\Gamma_m \ll \kappa$ , the correlation should reflect the Lorentzian response function of the optically damped harmonic oscillator, driven by an approximately white noise source. Fig. 3A shows a cross correlation measurement for device B, and for reference,  $S_{IS}(\omega) \times S_{IM}(\omega)$  is shown in the same plot, and the individual traces of  $S_{IS}$  and  $S_{IM}$  for these data are shown in Fig. 2. For a resonator well into the RPSN dominated regime, measured with ideal quantum efficiency, the two curves should coincide at the peak, yielding a perfect correlation. However, a white, uncorrelated measurement noise background, dominated by the meter beam's shot noise, separates the two curves away from the mechanical resonance. Additionally, the peak value of the cross correlation is smaller, arising mainly from two sources. The residual thermal motion is uncorrelated with the radiation pressure drive. Also, the imperfect detection efficiency of the signal laser leads to a loss of correlation, as information about the intracavity shot noise drive is unrecorded. We measure a peak relative correlation  $\mathcal{C}(\omega_m) = |S_{ISM}(\omega_m)|^2 / S_{IS}(\omega_m) S_{IM}(\omega_m) = 0.14$ . A simple estimate is  $\mathcal{C}(\omega_m) = R_S / (1 + R_S) \times \kappa_R / \kappa \times \epsilon_1 \times \epsilon_{\text{dark1}} = 0.15 \pm 0.02$ , where  $R_S / (1 + R_S) = 0.4 \pm 0.03$  is the fraction of the displacement spectrum due to RPSN,  $\kappa_R / \kappa = 0.59$  is the fraction of the light exiting the cavity through the output port,  $\epsilon_1 = 0.79 \pm 0.03$  is the post-cavity detection efficiency, and  $\epsilon_{\text{dark1}} = 0.8$  is due to dark noise on the photodetector. By intentionally adding white classical intensity noise of much larger amplitude than shot noise to the signal laser, we are able to demonstrate in Fig. 3B a (classical) relative cross correlation that approaches unity.

A detailed analysis of the cross correlation response yields considerable information about the system. Fig. 3C shows the phase of the correlation both with and without large classical intensity noise on the signal beam. Both show the 180 degree phase shift expected from the mechanical response. However, we also expect a phase offset of  $\arctan(2\omega_m/\kappa)$  between the classical noise dominated drive and the shot noise dominated drive (See Supplemental Material and Ref. [14]). Fitting these two curves yields a relative phase shift that is slightly smaller than predicted, implying that in our measurement with no intentionally added classical noise, about 75 % of the radiation pressure drive is from shot noise, in agreement with estimates obtained by directly measuring the classical noise level of the signal beam transmission spectrum.

If the signal beam is not precisely on resonance then the cross correlation will be distorted. Mechanical motion transduced directly onto the signal beam may either constructively or destructively add to the RPSN correlation depending on the sign of  $\Delta_S$ . By fitting the correlation data to the expected lineshape (see

Supplemental Material) with  $\Delta_S$  as a fit parameter, we estimate  $\Delta_S = 0.0003\kappa$ , which implies a contribution of only 3 % to the peak cross correlation from thermal motion. Also, note that since the thermal contribution is linear in  $\Delta_S$ , the effect of the few kilohertz residual technical fluctuations in the laser-cavity detuning should average to that of the mean value. We have also performed an experimental test to demonstrate the rejection of ambient motion from the cross correlation spectrum. Here, we mechanically excite the membrane with a white-noise driven piezoelectric actuator. As shown in Fig. 3B, the membrane is excited to a greater amplitude of motion near the mechanical resonance frequency. However, the cross correlation spectrum remains unchanged, implying very little of the ambient motion is transduced.

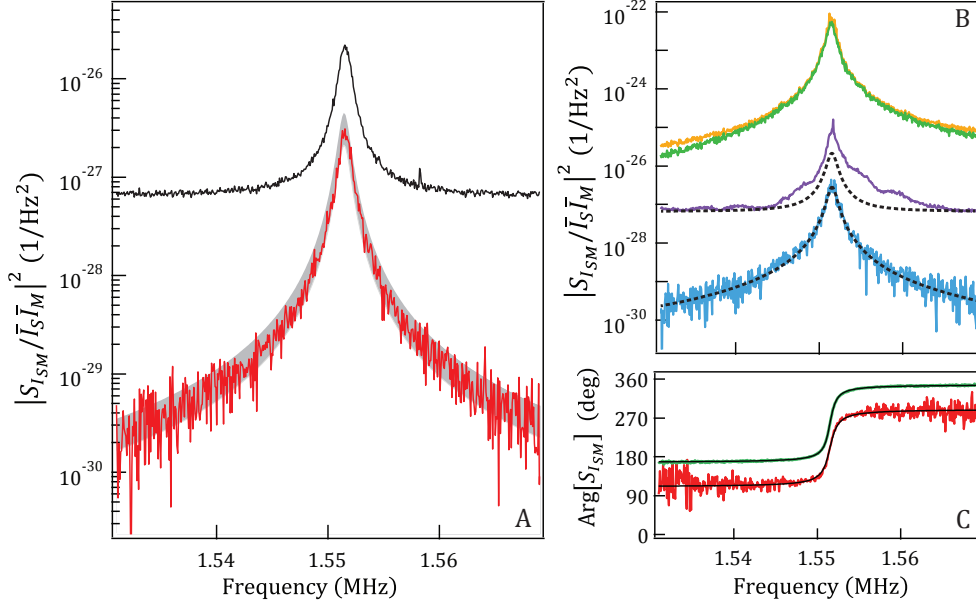


Figure 3: Cross correlation measurements. (A) The magnitude squared of  $S_{ISM}(\omega)/\bar{I}_S\bar{I}_M$  for device B (red), expected cross correlation including systematic uncertainty (gray),  $S_{IS}(\omega) \times S_{IM}(\omega)$  (black). Parameters are as listed in Fig. 1 caption except  $\Delta_S/2\pi = 300 \pm 100$  Hz,  $g/2\pi = 14.8 \pm 0.4$  Hz,  $N_S = 3.2 \times 10^8$  (B)  $S_{ISM}(\omega)$  (green) and,  $S_{IS}(\omega) \times S_{IM}(\omega)$  (orange) where classical intensity noise at the level of  $\sim 40$  times shot noise, is added to the signal beam,  $S_{ISM}(\omega)$  (blue)  $S_{IS}(\omega) \times S_{IM}(\omega)$  (purple) where membrane is driven with excess mechanical noise. Fits to the data of part (A) are displayed for reference (dashed black). (C) Phase of the cross correlation with classical intensity noise on signal beam (green) and without (red). Black curves are fits to the data.

An alternative interpretation of these cross correlation measurements is that of a QND measurement of the intracavity photon fluctuations of the signal beam [27]. Here, the membrane acts as the measurement device, with its state of motion recording the photon fluctuations over the band of the mechanical resonance. In fact our  $\mathcal{C}$  parameter is equivalent to the state preparation fidelity developed in Ref. [28] for nonideal QND measurements. Further, it has been shown that frequency-dependent ponderomotive squeezing of the signal beam quantum noise is possible [29], and such squeezing has recently been demonstrated in an atomic gas cavity optomechanical system [30]. However for the laser configuration used in these measurements ( $\Delta_S = 0$ ), we do not expect to see squeezing of the detected amplitude quadrature. In conclusion, we have

made several measurements of the effects of radiation pressure shot noise on a micromechanical resonator. These effects are signatures of quantum measurement back action from continuous position measurement by an optical probe. Our observations open the door to realizing position measurement near the SQL if residual thermal noise and excess cavity-laser phase noise can be eliminated. We have also demonstrated the parameters necessary for strong ponderomotive optical squeezing.

**Acknowledgments** We thank Pen-Li Yu for technical assistance and Konrad Lehnert’s group for helpful discussions. This work is supported by: DARPA QuASAR, ONR YIP, JILA NSF PFC. TP thanks the NRC for support. CR thanks the Clare Boothe Luce foundation for support.

## References

- [1] V.B. Braginskii and S.P. Vyatchanin. Gravitational waves and the limiting stability of self-excited oscillators. *Sov. Phys. JETP*, 47:433, Mar 1978.
- [2] Carlton M. Caves. Quantum-mechanical noise in an interferometer. *Phys. Rev. D*, 23:1693–1708, Apr 1981.
- [3] V. B. Braginsky and F. Y. Khalili. *Quantum Measurement*. Cambridge University Press, 1992.
- [4] I. Tittonen, G. Breitenbach, T. Kalkbrenner, T. Müller, R. Conradt, S. Schiller, E. Steinsland, N. Blanc, and N. F. de Rooij. Interferometric measurements of the position of a macroscopic body: Towards observation of quantum limits. *Phys. Rev. A*, 59:1038–1044, Feb 1999.
- [5] J. D. Teufel, T. Donner, M. A. Castellanos-Beltran, J. W. Harlow, and K. W. Lehnert. Nanomechanical motion measured with an imprecision below that at the standard quantum limit. *Nature Nanotechnology*, 4:820 – 823, Nov 2009.
- [6] G. Anetsberger, E. Gavartin, O. Arcizet, Q. P. Unterreithmeier, E. M. Weig, M. L. Gorodetsky, J. P. Kotthaus, and T. J. Kippenberg. Measuring nanomechanical motion with an imprecision below the standard quantum limit. *Phys. Rev. A*, 82:061804, Dec 2010.
- [7] Gregory M Harry and the LIGO Scientific Collaboration. Advanced ligo: the next generation of gravitational wave detectors. *Classical and Quantum Gravity*, 27(8):084006, 2010.
- [8] H. J. Kimble, Yuri Levin, Andrey B. Matsko, Kip S. Thorne, and Sergey P. Vyatchanin. Conversion of conventional gravitational-wave interferometers into quantum nondemolition interferometers by modifying their input and/or output optics. *Phys. Rev. D*, 65:022002, Dec 2001.
- [9] Vladimir B. Braginsky, Yuri I. Vorontsov, and Kip S. Thorne. Quantum nondemolition measurements. *Science*, 209:547–557, Aug 1980.
- [10] Kater W. Murch, Kevin L. Moore, Subhadeep Gupta, and Dan M. Stamper-Kurn. Observation of quantum-measurement backaction with an ultracold atomic gas. *Nature Physics*, 4:561 – 564, May 2008.
- [11] Nathan Brahms, Thierry Botter, Sydney Schreppler, Daniel W. C. Brooks, and Dan M. Stamper-Kurn. Optical detection of the quantization of collective atomic motion. *Phys. Rev. Lett.*, 108:133601, Mar 2012.

- [12] A. Heidmann, Y. Hadjar, and M. Pinard. Quantum nondemolition measurement by optomechanical coupling. *Applied Physics B: Lasers and Optics*, 64:173–180, 1997.
- [13] P. Verlot, A. Tavernarakis, T. Briant, P.-F. Cohadon, and A. Heidmann. Scheme to probe optomechanical correlations between two optical beams down to the quantum level. *Phys. Rev. Lett.*, 102:103601, Mar 2009.
- [14] K. Børkje, A. Nunnenkamp, B. M. Zwickl, C. Yang, J. G. E. Harris, and S. M. Girvin. Observability of radiation-pressure shot noise in optomechanical systems. *Phys. Rev. A*, 82:013818, Jul 2010.
- [15] Kazuhiro Yamamoto, Daniel Friedrich, Tobias Westphal, Stefan Gößler, Karsten Danzmann, Kentaro Somiya, Stefan L. Danilishin, and Roman Schnabel. Quantum noise of a michelson-sagnac interferometer with a translucent mechanical oscillator. *Phys. Rev. A*, 81:033849, Mar 2010.
- [16] Pierre Verlot et al. Towards the experimental demonstration of quantum radiation pressure noise. *C. R. Physique*, 12:826–836, 2011.
- [17] A. Naik, O. Buu, M. D. LaHaye, A. A. Clerk, A. D. Armour, M. P. Blencowe, and K. C. Schwab. Cooling a nanomechanical resonator with quantum back-action. *Nature*, 443:193–196, Sept 2006.
- [18] Farid Ya. Khalili, Haixing Miao, Huan Yang, Amir H. Safavi-Naeini, Oskar Painter, and Yanbei Chen. Quantum back-action in measurements of zero-point mechanical oscillations. 2012. arXiv:1206.0793.
- [19] J. D. Teufel, T. Donner, Dale Li, J. W. Harlow, M. S. Allman, K. Cicak, A. J. Sirois, J. D. Whittaker, K. W. Lehnert, and R. W. Simmonds. Sideband cooling of micromechanical motion to the quantum ground state. *Nature*, 475:359 – 363, July 2011.
- [20] Jasper Chan, T. P. Mayer Alegre, Amir H. Safavi-Naeini, Jeff T. Hill, Alex Krause, Simon Gröblacher, Markus Aspelmeyer, and Oskar Painter. Laser cooling of a nanomechanical oscillator into its quantum ground state. *Nature*, 478:89 – 92, Oct 2011.
- [21] E. Verhagen, S. Deléglise, S. Weis, A. Schliesser, and T. J. Kippenberg. Quantum-coherent coupling of a mechanical oscillator to an optical cavity mode. *Nature*, 482:63 – 67, Feb 2012.
- [22] J. D. Thompson, B. M. Zwickl, A. M. Jayich, Florian Marquardt, S. M. Girvin, and J. G. E. Harris. Strong dispersive coupling of a high-finesse cavity to a micromechanical membrane. *Nature*, 452:72–75, Mar 2008.
- [23] D. J. Wilson, C. A. Regal, S. B. Papp, and H. J. Kimble. Cavity optomechanics with stoichiometric SiN films. *Phys. Rev. Lett.*, 103:207204, Nov 2009.
- [24] T. P. Purdy, R. W. Peterson, P.-L. Yu, and C. A. Regal. Cavity optomechanics with Si<sub>3</sub>N<sub>4</sub> membranes at cryogenic temperatures. *New Journal of Physics*, 2012. accepted, Preprint available as arXiv:1208.6560.
- [25] Florian Marquardt, Joe P. Chen, A. A. Clerk, and S. M. Girvin. Quantum theory of cavity-assisted sideband cooling of mechanical motion. *Phys. Rev. Lett.*, 99:093902, Aug 2007.
- [26] I. Wilson-Rae, N. Nooshi, W. Zwerger, and T. J. Kippenberg. Theory of ground state cooling of a mechanical oscillator using dynamical backaction. *Phys. Rev. Lett.*, 99:093901, Aug 2007.
- [27] K. Jacobs, P. Tombesi, M. J. Collett, and D. F. Walls. Quantum-nondemolition measurement of photon number using radiation pressure. *Phys. Rev. A*, 49:1961–1966, Mar 1994.



- [28] M. J. Holland, M. J. Collett, D. F. Walls, and M. D. Levenson. Nonideal quantum nondemolition measurements. *Phys. Rev. A*, 42:2995–3005, Sep 1990.
- [29] C. Fabre, M. Pinard, S. Bourzeix, A. Heidmann, E. Giacobino, and S. Reynaud. Quantum-noise reduction using a cavity with a movable mirror. *Phys. Rev. A*, 49:1337–1343, Feb 1994.
- [30] Daniel W. C. Brooks, Thierry Botter, Sydney Schreppler, Thomas P. Purdy, Nathan Brahms, and Dan M. Stamper-Kurn. Non-classical light generated by quantum-noise-driven cavity optomechanics. *Nature*, 448:476–480, Aug 2012.

Supplementary Materials for:  
 “Observation of Radiation Pressure Shot Noise”  
 T. P. Purdy, R. W. Peterson, and C. A. Regal

## S.1 Theory

Here we calculate the response of an optomechanical system to two independent laser driving fields. Additionally, we compute the spectrum of the two time cross correlation of the photocurrents of the transmitted laser fields. This formalism is used to model our membrane cavity optomechanical system, as well as our specific detection setup that incorporates direct photodetection of the transmitted intensity of both laser fields. A schematic of the experiment is given in Fig. S4.

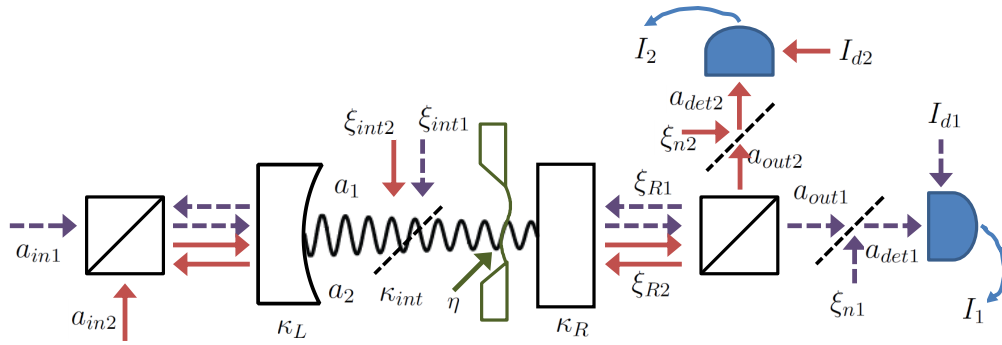


Figure S4: Cavity optomechanical probing and detection setup. Two orthogonally polarized beams, laser 1 (dashed purple) and laser 2 (solid red) propagate through the system. Boxes represent polarizing beam splitters. Dashed lines indicate optical loss ports. Photodetectors are in blue. Various operators are labeled in accordance with the text.

### S.1.1 Equations of Motion

We start from a Hamiltonian  $H = H_0 + H_\kappa + H_\Gamma$  describing the mechanical and optical evolution, dissipation and interactions [14]:

$$H_0 = \hbar\omega_m c^\dagger c + \hbar\omega_c a_1^\dagger a_1 + \hbar\omega_c a_2^\dagger a_2 + \hbar G_1 Z_{zp}(c + c^\dagger)a_1^\dagger a_1 + \hbar G_2 Z_{zp}(c + c^\dagger)a_2^\dagger a_2 \quad (S1)$$

where  $\omega_m$  is the mechanical resonance frequency,  $c$  is the annihilation operator for the mechanical resonator,  $\omega_c$  is the cavity resonance frequency, and  $a_1, a_2$  are annihilation operators for the two polarizations of the cavity mode.  $G_1, G_2$  are the optomechanical coupling constants,  $Z_{zp} = \sqrt{\hbar/2m\omega_m}$  is the oscillator zero point motion, where  $m$  is resonator’s effective mass. Single photon optomechanical coupling rates are  $g_1 = G_1 Z_{zp}$ ,  $g_2 = G_2 Z_{zp}$ .  $H_\kappa$  represents the optical input and output coupling, and  $H_\Gamma$  represents the coupling to the mechanical bath. We will eventually specify the results of our calculation to identify the parameters of laser 1 with the signal beam ( $_S$ ) and laser 2 with the meter beam ( $_M$ ) of the experiment. The Heisenberg Langevin

equations of motion are:

$$\begin{aligned}
\dot{a}_1(t) &= -\frac{\imath}{\hbar} [a_1(t), H_0] - \frac{\kappa}{2} a_1(t) + \sqrt{\kappa_L} a_{\text{inL1}}(t) + \sqrt{\kappa_{\text{int}}} a_{\text{int1}}(t) + \sqrt{\kappa_R} a_{\text{inR1}} \\
\dot{a}_2(t) &= -\frac{\imath}{\hbar} [a_2(t), H_0] - \frac{\kappa}{2} a_2(t) + \sqrt{\kappa_L} a_{\text{inL2}}(t) + \sqrt{\kappa_{\text{int}}} a_{\text{int2}}(t) + \sqrt{\kappa_R} a_{\text{inR2}} \\
\dot{c}(t) &= -\frac{\imath}{\hbar} [c(t), H_0] + \sqrt{\Gamma_0} \eta(t)
\end{aligned} \tag{S2}$$

We have introduced a Langevin noise operator  $\eta(t)$  to model the thermal mechanical bath, with mechanical decay rate  $\Gamma_0$ . Additionally, we include input optical field operators for the three coupling channels of each cavity mode, input mirror  $\kappa_L$ , internal loss  $\kappa_{\text{int}}$ , and output mirror  $\kappa_R$ . We assume the cavity couplings are identical for both optical modes. By introducing the definitions for the optical field operators we find:

$$\begin{aligned}
a_1(t) &= (\bar{a}_1 + d_1(t))e^{-\imath\omega_1 t}, \quad a_2(t) = (\bar{a}_2 + d_2(t))e^{-\imath\omega_2 t} \\
a_{\text{inL1}}(t) &= (\bar{a}_{\text{in1}} + \xi_{L1}(t) + dx_1(t))e^{\imath\omega_1 t}, \quad a_{\text{inL2}}(t) = (\bar{a}_{\text{in2}} + \xi_{L2}(t))e^{\imath\omega_2 t} \\
a_{\text{inR1}}(t) &= \xi_{R1}(t)e^{\imath\omega_1 t}, \quad a_{\text{inR2}}(t) = \xi_{R2}(t)e^{\imath\omega_2 t} \\
a_{\text{int1}}(t) &= \xi_{\text{int1}}(t)e^{\imath\omega_1 t}, \quad a_{\text{int2}}(t) = \xi_{\text{int2}}(t)e^{\imath\omega_2 t}
\end{aligned}$$

We allow for coherent field inputs from the left with real valued amplitudes  $\bar{a}_{\text{in1}} = \langle a_{\text{in1}} \rangle$ ,  $\bar{a}_{\text{in2}} = \langle a_{\text{in2}} \rangle$  and frequencies  $\omega_1, \omega_2$ , as well as vacuum noise inputs on all ports from the Langevin noise operators  $\xi$ , labeled by subscripts indicating the port and laser mode. Classical input intensity noise on laser 1 is modeled with the real valued classical noise operator  $dx_1$ , which is measured in units relative to the shot noise level.  $\bar{a}_1, \bar{a}_2$  represent the complex valued classical amplitude of the intracavity field modes, while the operators  $d_1, d_2$  represent the small classical and quantum fluctuations of the intracavity field.  $z = Z_{\text{zp}}(c + c^\dagger) - \bar{z}$  is the displacement operator, defined so the mechanical coordinate is centered around the optomechanically shifted equilibrium location  $\bar{z}$ .  $\Delta_1 = \omega_c - \omega_1 + G_1 \bar{z}$  and  $\Delta_2 = \omega_c - \omega_2 + G_2 \bar{z}$  represent the input laser detuning from the optomechanically shifted cavity resonance. The equations of motion are linearized by neglecting small terms of order  $d^2, d \times z$ . To solve the equations of motion we Fourier transform the Eqns. S2 according to the following conventions:  $f(\omega) \equiv \int_{-\infty}^{\infty} e^{\imath\omega t} f(t) dt$ ,  $f^\dagger(\omega) \equiv \int_{-\infty}^{\infty} e^{\imath\omega t} f^\dagger(t) dt$ ,  $(f^\dagger(\omega))^\dagger = f(-\omega)$ .

$$\begin{aligned}
d_1(\omega) &= \chi_{c1}(\omega) (-\imath G_1 \bar{a}_1 z(\omega) + \zeta_1(\omega)) \\
d_2(\omega) &= \chi_{c2}(\omega) (-\imath G_2 \bar{a}_2 z(\omega) + \zeta_2(\omega)) \\
\frac{z(\omega)}{Z_{\text{zp}}} &= \frac{1}{\mathcal{N}(\omega)} \left( -2\omega_m (\bar{a}_1^* g_1 \chi_{c1}(\omega) \zeta_1(\omega) + \bar{a}_1 g_1 \chi_{c1}^*(-\omega) \zeta_1^\dagger(\omega) + \bar{a}_2^* g_2 \chi_{c2}(\omega) \zeta_2(\omega) \right. \\
&\quad \left. + \bar{a}_2 g_2 \chi_{c2}^*(-\omega) \zeta_2^\dagger(\omega)) + \sqrt{\Gamma_0} \left( \frac{\eta(\omega)}{\chi_m^*(-\omega)} + \frac{\eta^\dagger(\omega)}{\chi_m(\omega)} \right) \right)
\end{aligned}$$

We have introduced the mechanical susceptibility  $\chi_m(\omega) = (\Gamma_0/2 - \imath(\omega - \omega_m))^{-1}$ , and the cavity susceptibilities for the two modes  $\chi_{c1}(\omega) = (\kappa/2 - \imath(\omega + \Delta_1))^{-1}$  and  $\chi_{c2}(\omega) = (\kappa/2 - \imath(\omega + \Delta_2))^{-1}$ . The optical noise operators are lumped into  $\zeta_1(\omega) = \sqrt{\kappa_L} \xi_{L1}(\omega) + dx_1(\omega) + \sqrt{\kappa_R} \xi_{R1}(\omega) + \sqrt{\kappa_{\text{int}}} \xi_{\text{int1}}(\omega)$  and  $\zeta_2(\omega) = \sqrt{\kappa_L} \xi_{L2}(\omega) + \sqrt{\kappa_R} \xi_{R2}(\omega) + \sqrt{\kappa_{\text{int}}} \xi_{\text{int2}}(\omega)$ . The function  $\mathcal{N}(\omega) = (\chi_m(\omega) \chi_m^*(-\omega))^{-1} - 2\omega_m Z_{\text{zp}}^2 (|\bar{a}_1|^2 G_1^2 \Pi_1(\omega) + |\bar{a}_2|^2 G_2^2 \Pi_2(\omega))$  modifies the mechanical susceptibility and  $\Pi_1(\omega) = \chi_{c1}(\omega) - \chi_{c1}^*(-\omega)$ ,  $\Pi_2(\omega) = \chi_{c2}(\omega) - \chi_{c2}^*(-\omega)$ .

The two-sided mechanical displacement spectrum  $S_z^{(2)}(\omega) = \langle z(-\omega)z(\omega) \rangle$  may then be calculated from the expectation values of the operator pairs:

$$\begin{aligned}\langle \xi_{L1}(-\omega)\xi_{L1}^\dagger(\omega) \rangle &= \langle \xi_{\text{int}1}(-\omega)\xi_{\text{int}1}^\dagger(\omega) \rangle = \langle \xi_{R1}(-\omega)\xi_{R1}^\dagger(\omega) \rangle = 1 \\ \langle \xi_{L2}(-\omega)\xi_{L2}^\dagger(\omega) \rangle &= \langle \xi_{\text{int}2}(-\omega)\xi_{\text{int}2}^\dagger(\omega) \rangle = \langle \xi_{R2}(-\omega)\xi_{R2}^\dagger(\omega) \rangle = 1 \\ \langle \eta(-\omega)\eta^\dagger(\omega) \rangle &= n_{\text{th}} + 1, \quad \langle \eta^\dagger(-\omega)\eta(\omega) \rangle = n_{\text{th}} \\ \langle dx_1(-\omega)dx_1(\omega) \rangle &= B_1\end{aligned}$$

Here  $n_{\text{th}}$  is the thermal occupation of the mechanical oscillator, and all other expectation values of products of Langevin operators are zero. The classical intensity noise is assumed to be locally white and takes a value  $B_1$  times that of shot noise. Here we assume the Langevin operators as well as the displacement spectrum are delta function correlated i.e.  $\langle \xi(-\omega')\xi(\omega) \rangle = \delta(\omega - \omega')$  with assumed integration over  $\omega'$  for the calculation of all experimentally relevant quantities.

$$\begin{aligned}\frac{S_z^{(2)}(\omega)}{Z_{\text{zp}}^2} &= \frac{1}{|\mathcal{N}(\omega)|^2} \left( \Gamma_0 \left( \frac{n_{\text{th}} + 1}{|\chi_m(\omega)|^2} + \frac{n_{\text{th}}}{|\chi_m(-\omega)|^2} \right) \right. \\ &\quad + 4\omega_m^2 \kappa |\bar{a}_1 g_1 \chi_{c1}(-\omega)|^2 + 4\omega_m^2 \kappa |\bar{a}_2 g_2 \chi_{c2}(-\omega)|^2 \\ &\quad \left. + 4\omega_m^2 \kappa_L |\bar{a}_1 g_1 (\chi_{c1}(\omega) + \chi_{c1}^*(-\omega))|^2 B_1 \right) \quad (\text{S3})\end{aligned}$$

The displacement spectrum consists of four terms. The first term represents the residual thermal motion of the optically cooled oscillator. The second term is the displacement due to RPSN from laser 1. Assuming laser 2 is responsible for the majority of the optical damping, the third term contains most of the oscillator's zero point motion as well as the small RPSN effect from laser 2. The last term is the response to classical intensity noise on laser 1.

Given the classical and quantum fluctuations in the optical spectrum, we want to calculate the mechanical response. Let us assume  $\Delta_1 \sim 0$ , as is the case in the actual experiment. Then  $A^{\text{sn}} = (\kappa_R \bar{a}^* \bar{a})^{-1}$  is the output relative intensity spectrum of laser 1 due to shot noise, and  $A^{\text{cn}} = \kappa_L |\chi_{c1}(\omega) + \chi_{c1}^*(-\omega)|^2 B_1 / (\bar{a}^* \bar{a})$  is the output relative intensity spectrum of laser 1 due to classical intensity noise. The classical output noise reflects filtering by the Lorentzian cavity response, whereas full shot noise appears on the output light. However, inside the cavity the shot noise intensity fluctuations are suppressed by the cavity Lorentzian [25]. Thus we must treat the perceived level of classical and shot noise differently to correctly infer the mechanical response. Using Eq. S3 we find that  $S_z^{\text{sn}}/S_z^{\text{cn}} = \kappa \kappa_R |\chi_{c1}(-\omega)|^2 A^{\text{sn}}/A^{\text{cn}}$ . Here  $S_z^{\text{sn}}$  and  $S_z^{\text{cn}}$  are the contribution to the displacement spectrum from the shot and classical noise on laser 1, equal to the second and fourth terms of Eq. S3 respectively. Experimentally this means that even when the measured classical intensity noise at an output photodetector is only a few percent of the shot noise level, it may still represent a significant amount of radiation pressure drive compared to the shot noise drive.

### S.1.2 Correlation Spectrum

We next turn to the computation of the photocurrent cross correlation spectrum,  $S_{I_{12}}^{(2)}(\omega) = \langle (I_1(-\omega) - \bar{I}_1)(I_2(\omega) - \bar{I}_2) \rangle_s$ , with the mean photocurrents  $\bar{I}_1 = \langle I_1(t) \rangle$ ,  $\bar{I}_2 = \langle I_2(t) \rangle$ . Since the photocurrents are classical commuting variables, it should be that  $I_1(\omega) \times I_2(\omega) = I_2(\omega) \times I_1(\omega)$ . To ensure

this classical property, we compute the symmetrized expectation value for  $S_{I_{12}}$ , defining  $\langle f(\omega)g(\omega) \rangle_s = (1/2)(\langle f(\omega)g(\omega) \rangle + \langle g(\omega)f(\omega) \rangle)$ . For comparison with experimental data we compute the one-sided power spectrum  $S_{I_{12}}(\omega) = S_{I_{12}}^{(2)}(\omega) + S_{I_{12}}^{(2)}(-\omega)$ . The photocurrents are given by

$$I_1(t) = \hbar\omega_1 \mathcal{R}_1 a_{\text{det1}}^\dagger(t) a_{\text{det1}}(t) + I_{d1}(t), \quad I_2(t) = \hbar\omega_2 \mathcal{R}_2 a_{\text{det2}}^\dagger(t) a_{\text{det2}}(t) + I_{d2}(t)$$

where  $I_{d1}$ ,  $I_{d2}$  are photodetector dark currents,  $\mathcal{R}_1 = q_e \epsilon_1 / \hbar\omega_1$ ,  $\mathcal{R}_2 = q_e \epsilon_2 / \hbar\omega_2$  are the photodetector sensitivities (with  $q_e$  the photoelectron charge) and  $\epsilon_1$ ,  $\epsilon_2$  include the photodetector quantum efficiencies and propagation losses outside of the cavity.  $a_{\text{det1}}$  and  $a_{\text{det2}}$  are the photon annihilation operators at the photodetector (see Figure S4). The fields at the detector are a combination of the transmitted cavity fields,  $a_{\text{out1}}$ ,  $a_{\text{out2}}$  and vacuum noise from the optical loss channels. Using the definitions  $a_{\text{out1}}(t) = (\bar{a}_{\text{out1}} + d_{\text{out1}}(t))e^{i\omega_1 t}$ ,  $a_{\text{out2}}(t) = (\bar{a}_{\text{out2}} + d_{\text{out2}}(t))e^{i\omega_2 t}$  to distinguish the small fluctuations from the large classical amplitude  $\bar{a}_{\text{out1}} = \langle a_{\text{out1}}(t) \rangle$ ,  $\bar{a}_{\text{out2}} = \langle a_{\text{out2}}(t) \rangle$ , we find:

$$a_{\text{det1}}^\dagger(t) a_{\text{det1}}(t) = \epsilon_1 \bar{a}_{\text{out1}}^* \bar{a}_{\text{out1}} + \epsilon_1 (\bar{a}_{\text{out1}}^* d_{\text{out1}}(t) + \bar{a}_{\text{out1}} d_{\text{out1}}^\dagger(t)) + \sqrt{\epsilon_1(1-\epsilon_1)} (\bar{a}_{\text{out1}}^* \xi_{n1}(t) + \bar{a}_{\text{out1}} \xi_{n1}^\dagger(t))$$

$$a_{\text{det2}}^\dagger(t) a_{\text{det2}}(t) = \epsilon_2 \bar{a}_{\text{out2}}^* \bar{a}_{\text{out2}} + \epsilon_2 (\bar{a}_{\text{out2}}^* d_{\text{out2}}(t) + \bar{a}_{\text{out2}} d_{\text{out2}}^\dagger(t)) + \sqrt{\epsilon_2(1-\epsilon_2)} (\bar{a}_{\text{out2}}^* \xi_{n2}(t) + \bar{a}_{\text{out2}} \xi_{n2}^\dagger(t))$$

where  $\xi_{n1}$ ,  $\xi_{n2}$  are Langevin vacuum noise operators. Substituting in the above relations, we find:

$$\frac{S_{I_{12}}^{(2)}(\omega)}{\bar{I}_1 \bar{I}_2} = \left\langle \left( \frac{\bar{a}_{\text{out1}}^* d_{\text{out1}}(-\omega) + \bar{a}_{\text{out1}} d_{\text{out1}}^\dagger(-\omega)}{\bar{a}_{\text{out1}}^* \bar{a}_{\text{out1}}} \right) \left( \frac{\bar{a}_{\text{out2}}^* d_{\text{out2}}(\omega) + \bar{a}_{\text{out2}} d_{\text{out2}}^\dagger(\omega)}{\bar{a}_{\text{out2}}^* \bar{a}_{\text{out2}}} \right) \right\rangle_s$$

where we have employed the fact that  $I_{d1}$ ,  $I_{d2}$ ,  $\xi_{n1}$ ,  $\xi_{n2}$  are all uncorrelated with each other. Thus terms proportional to expectation values of products of these operators are zero, and  $S_{I_{12}}^{(2)}(\omega)/\bar{I}_1 \bar{I}_2$  becomes independent of  $\epsilon_1$ ,  $\epsilon_2$ . We note, however, the power spectra of the individual photocurrents will depend on  $I_{d1}$ ,  $I_{d2}$ ,  $\epsilon_1$ ,  $\epsilon_2$ , so the ratio  $S_{I_{12}}/S_{I_1} S_{I_2}$  does improve with increasing detection efficiency and a lower photodetector noise floor. We can relate the intracavity photon operators to the output operators using the boundary conditions  $\bar{a}_{\text{out1}} = \sqrt{\kappa_R} \bar{a}_1$ ,  $\bar{a}_{\text{out2}} = \sqrt{\kappa_R} \bar{a}_2$ , and  $d_{\text{out1}} = \sqrt{\kappa_R} d_1 - \xi_{R1}$ ,  $d_{\text{out2}} = \sqrt{\kappa_R} d_2 - \xi_{R2}$ . Applying the

solution to the equations of motion from above, we find:

$$\begin{aligned}
\frac{S_{I_{12}}^{(2)}(\omega)}{\bar{I}_1 \bar{I}_2} &= \frac{-1}{\kappa_R |\bar{a}_1|^2 |\bar{a}_2|^2} \times \\
&\left( \begin{aligned}
&\sqrt{\kappa_R} G_1 |\bar{a}_1|^2 \Pi_1(-\omega) \sqrt{\kappa_R} G_2 |\bar{a}_2|^2 \Pi_2(\omega) \langle z(-\omega) z(\omega) \rangle_s \\
&+ \sqrt{\kappa_R} G_1 |\bar{a}_1|^2 i \Pi_1(-\omega) \bar{a}_2^* \sqrt{\kappa_L \kappa_R} \chi_{c2}(\omega) \langle z(-\omega) \xi_{L2}(\omega) \rangle_s \\
&+ \sqrt{\kappa_R} G_1 |\bar{a}_1|^2 i \Pi_1(-\omega) \bar{a}_2^* \sqrt{\kappa_{\text{int}} \kappa_R} \chi_{c2}(\omega) \langle z(-\omega) \xi_{\text{int}2}(\omega) \rangle_s \\
&+ \sqrt{\kappa_R} G_1 |\bar{a}_1|^2 i \Pi_1(-\omega) \bar{a}_2^* (\kappa_R \chi_{c2}(\omega) - 1) \langle z(-\omega) \xi_{R2}(\omega) \rangle_s \\
&+ \sqrt{\kappa_R} G_1 |\bar{a}_1|^2 i \Pi_1(-\omega) \bar{a}_2 \sqrt{\kappa_L \kappa_R} \chi_{c2}^*(-\omega) \langle z(-\omega) \xi_{L2}^\dagger(\omega) \rangle_s \\
&+ \sqrt{\kappa_R} G_1 |\bar{a}_1|^2 i \Pi_1(-\omega) \bar{a}_2 \sqrt{\kappa_{\text{int}} \kappa_R} \chi_{c2}^*(-\omega) \langle z(-\omega) \xi_{\text{int}2}^\dagger(\omega) \rangle_s \\
&+ \sqrt{\kappa_R} G_1 |\bar{a}_1|^2 i \Pi_1(-\omega) \bar{a}_2 (\kappa_R \chi_{c2}^*(-\omega) - 1) \langle z(-\omega) \xi_{R2}^\dagger(\omega) \rangle_s \\
&+ \sqrt{\kappa_R} G_2 |\bar{a}_2|^2 i \Pi_2(\omega) \bar{a}_1^* \sqrt{\kappa_L \kappa_R} \chi_{c1}(-\omega) (\langle \xi_{L1}(-\omega) z(\omega) \rangle_s + \langle dx_1(-\omega) z(\omega) \rangle_s) \\
&+ \sqrt{\kappa_R} G_2 |\bar{a}_2|^2 i \Pi_2(\omega) \bar{a}_1^* \sqrt{\kappa_{\text{int}} \kappa_R} \chi_{c1}(-\omega) \langle \xi_{\text{int}1}(-\omega) z(\omega) \rangle_s \\
&+ \sqrt{\kappa_R} G_2 |\bar{a}_2|^2 i \Pi_2(\omega) \bar{a}_1^* (\kappa_R \chi_{c1}(-\omega) - 1) \langle \xi_{R1}(-\omega) z(\omega) \rangle_s \\
&+ \sqrt{\kappa_R} G_2 |\bar{a}_2|^2 i \Pi_2(\omega) \bar{a}_1 \sqrt{\kappa_L \kappa_R} \chi_{c1}^*(\omega) (\langle \xi_{L1}^\dagger(-\omega) z(\omega) \rangle_s + \langle dx_1(-\omega) z(\omega) \rangle_s) \\
&+ \sqrt{\kappa_R} G_2 |\bar{a}_2|^2 i \Pi_2(\omega) \bar{a}_1 \sqrt{\kappa_{\text{int}} \kappa_R} \chi_{c1}^*(\omega) \langle \xi_{\text{int}1}^\dagger(-\omega) z(\omega) \rangle_s \\
&+ \sqrt{\kappa_R} G_2 |\bar{a}_2|^2 i \Pi_2(\omega) \bar{a}_1 (\kappa_R \chi_{c1}^*(\omega) - 1) \langle \xi_{R1}^\dagger(-\omega) z(\omega) \rangle_s
\end{aligned} \right) \quad (\text{S4})
\end{aligned}$$

The necessary operator expectation values are:

$$\begin{aligned}
\langle z(-\omega) \xi_{j2}(\omega) \rangle_s &= \frac{-\omega_m \sqrt{\kappa_j}}{\mathcal{N}(-\omega)} g_2 Z_{\text{zp}} \bar{a}_2 \chi_{c2}^*(\omega), \quad \text{for } j = L, \text{int}, R \\
\langle \xi_{j1}(-\omega) z(\omega) \rangle_s &= \frac{-\omega_m \sqrt{\kappa_j}}{\mathcal{N}(\omega)} g_1 Z_{\text{zp}} \bar{a}_1 \chi_{c1}^*(-\omega), \quad \text{for } j = L, \text{int}, R \\
\langle dx_1(-\omega) z(\omega) \rangle_s &= \frac{-2\omega_m \sqrt{\kappa_L}}{\mathcal{N}(\omega)} g_1 Z_{\text{zp}} (\bar{a}_1^* \chi_{c1}(\omega) + \bar{a}_1 \chi_{c2}^*(-\omega)) B_1
\end{aligned}$$

To understand which terms are relevant in the experiment for RPSN, we note that  $\Pi_1(\omega)$  approaches zero as  $\Delta_1$  approaches zero. The first seven terms of Eq. S4 then vanish under these conditions. This leaves terms that are proportional to correlations between  $z$ , the resonator position, and vacuum noise operators  $\xi_{L1}$ ,  $\xi_{R1}$  which represent the shot noise optical driving force on laser 1. In the limit where  $\Delta_1 = 0$  and in the absence of classical intensity noise, the cross correlation takes a simple form  $\frac{S_{I_{12}}^{(2)}(\omega)}{\bar{I}_1 \bar{I}_2} = 2i g_1 g_2 \omega_m \frac{\Pi_2(\omega) \chi_{c1}^*(\omega)}{\mathcal{N}(\omega)}$ .

For classical intensity noise an additional term is added:  $2i g_1 g_2 \omega_m \kappa_L \frac{\Pi_2(\omega) |\chi_{c1}(\omega) + \chi_{c1}^*(-\omega)|^2}{\mathcal{N}(\omega)} B_1$ . Note that in our case where  $\Gamma_m \ll \kappa$ , the classical and shot noise terms show similar functional form near  $\omega = \omega_m$ . Importantly, the shot noise driven term includes an extra phase shift of  $\text{Arg}(\chi_{c1}^*(\omega_m)) \sim \arctan(2\omega_m/\kappa)$ . This additional phase shift allows one to experimentally distinguish the quantum versus classical origin of a

radiation pressure drive. As shown in Figure S5B, the phase offset in the cross correlation varies continuously as the classical noise level is increased relative to the shot noise level.

When  $\Delta_1$  is nonzero, the first term of Eq. S4 produces a correlation induced by the mechanical motion of the resonator imprinted onto both photocurrents. Depending on the sign of  $\Delta_1$  the correlation from thermal motion may add either constructively or destructively with the RPSN correlation, leading to a laser frequency dependent lineshape. Example expected cross correlation lineshapes are presented in Fig. S5A. Note that this effect is most pronounced near the mechanical resonance peak. Over a wide range of  $\Delta_1$  the Lorentzian wings of the mechanical resonance are insensitive to the thermal motion and give an accurate representation of the RPSN correlation.

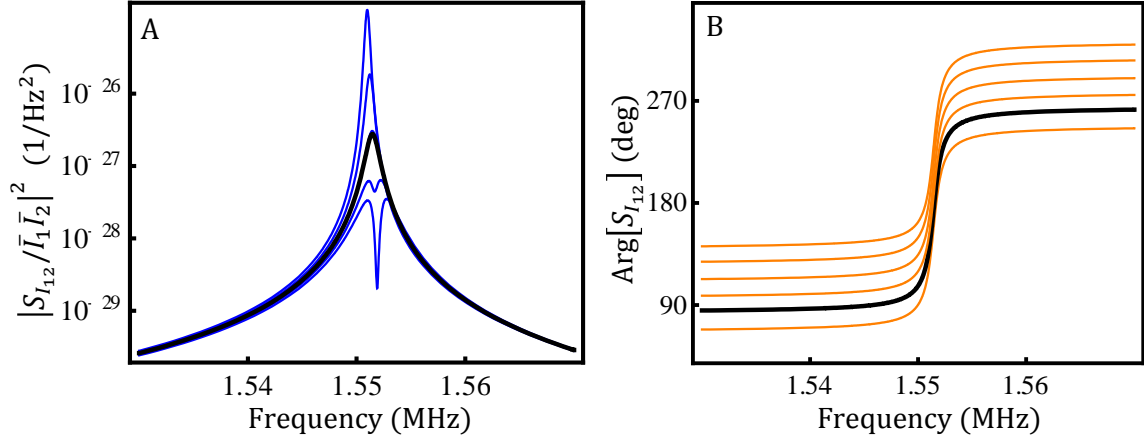


Figure S5: Cross correlation spectra. The magnitude squared (A) and the phase (B) of  $S_{I_{12}}$  (described as  $S_{I_{SM}}$  in the main text) are plotted for the parameters of device B. In (A)  $\Delta_1$  is varied. The tallest curve corresponds to  $\Delta_1/2\pi = 10$  kHz, and the lowest curve to -10 kHz. The black curve corresponds to the 0.28 kHz, the value of the correlation measurement in Fig 3A. In (A) the level of classical intensity noise relative to shot noise on laser 1 is varied. The bottom curve is pure quantum noise and the top curve is pure classical noise. The black curve corresponds to a measured noise at the photodetector consisting of 91% shot noise (75% of radiation pressured drive from shot noise) in the correlation measurement shown in Fig. 3A.

### S.1.3 Optical Bistability

One limit to the amount of optical power circulating in an optomechanical system is the onset of optomechanical bistability. Here, the mean radiation pressure on the mechanical element causes a static displacement, which shifts the cavity resonance frequency by  $\sim G_1\bar{z}$ . When this shift becomes comparable to the cavity linewidth, there exist two stable values of the circulating power and  $\bar{z}$  for a given input optical power, over some range of laser frequencies where the laser is nearly resonant with the cavity. In this situation the system may be driven by small noise sources from one stable equilibrium to the other in an uncontrolled fashion. To some extent, such processes can be avoided by using active feedback, as is employed in the actual experiment, increasing the duration of stable operation. To estimate the threshold for optomechanical bistability, we need to consider the net displacement of all the mechanical modes of our system with appreciable optomechanical coupling, not just the mode of interest for RPSN measurements. The critical

value of the intracavity photon occupation,  $N_1^c$ , above which bistable behavior is observed may be estimated for our membrane system by:

$$N_1^c \sim \sum_{m,n} \frac{0.77 \kappa m \omega_{(m,n)}^2}{\hbar G_{(m,n)}^2}$$

Here the sum is over mechanical eigenmode indices  $(m, n)$ , and  $\omega_{(m,n)}$ ,  $G_{(m,n)}$  are the mechanical resonance frequency and optomechanical coupling constant for the mode  $(m, n)$ . We estimate  $G_{(m,n)}$  by measuring the location of the optical mode spot on the membrane, and then computing overlap integrals between the expected optical and mechanical mode functions for each mechanical mode. For our measured parameters we obtain  $N_1^c \sim 3.5 \times 10^8$  which is comparable to the highest value of  $N_S$  employed in the actual experiment.

## S.2 Experimental Methods

Here we describe in detail the calibration and operation of our optomechanical system. More details about the construction of the system can be found in Ref. [24].

### S.2.1 Experimental setup

The optical cavity consist of two mirrors, one flat, one with a 5 cm radius of curvature, both with approximately  $1 \times 10^{-4}$  fractional intensity transmission at the operating wavelength of 1064 nm and only a few  $\times 10^{-6}$  scattering and absorption losses. The mirrors are held at a separation  $L = 5.1$  mm by an invar spacer. With this geometry, the cavity is expected to support a Gaussian profile standing wave mode with a  $1/e^2$  intensity radius of 72  $\mu\text{m}$ . The flat mirror is attached to the invar spacer through a multilayer piezoactuator that is used to precisely tune the overall optical path length of the cavity. The empty cavity finesse is measured to be 31,000 via optical ringdown spectroscopy.

A stoichiometric high-tensile-stress  $\text{Si}_3\text{N}_4$  membrane supplied by Norcada Inc. is placed inside the cavity as the mechanical element. The membrane is square in shape, 0.5 mm on a side and is suspended on a silicon frame with dimensions 5 mm  $\times$  5 mm  $\times$  0.5 mm. The membrane film is typically measured via ellipsometry to have a refractive index of 2.0 and film thickness of 40 nm, yielding a reflectivity of 10 % for 1064 nm light. The mechanical modes that most strongly couple to the light are transverse “drumhead” modes, which in the high-tension limit, show sinusoidal displacement profiles, with motion out of the plane of membrane. We label the modes with two indices (i,j) denoting the number of antinodes of oscillation along each of the transverse direction. For most of the experiments performed we focus on the (2,2) mode which has four antinodes, one in each corner of the membrane. This mode oscillates at a frequency  $\omega_m/2\pi \sim 1.55$  MHz, which is twice the frequency of the fundamental (1,1) mode. The intrinsic mechanical linewidth, which varies with temperature and mounting technique, is measured in-situ, at a wavelength where the cavity finesse is low to avoid any optomechanical effects, via mechanical ringdown spectroscopy, giving  $\Gamma_0/2\pi = 0.116$  Hz for device A and  $\Gamma_0/2\pi = 0.47$  Hz for device B.

The membrane is positioned in the cavity, so that the optical mode spot is approximately aligned with one of the antinodes of the (2,2) membrane mode to attain the largest optomechanical coupling. The membrane is located about 0.9 mm from the flat mirror, and its position can be finely tuned along the optical standing wave with another multilayer piezoactuator. The effective cavity input and output coupling and loss as well as the optomechanical coupling all vary with the location of the membrane along the optical axis. In conjunction with a simple matrix model [23], we use optical ringdown measurements of the cavity linewidth when the membrane is placed at the operating point to extract values for the cavity parameters. We determine  $\kappa$  the total cavity linewidth,  $\kappa_L$  and  $\kappa_R$ , the input and output coupling of the cavity, and



$\kappa_{\text{int}}$ , the internal cavity loss coupling.  $\kappa_{\text{int}}$  is due mainly to membrane absorption and scattering as well as clipping of the optical mode by the membrane frame. This analysis yields  $\kappa/2\pi=1.17$  MHz,  $\kappa_L = 0.33\kappa$ ,  $\kappa_R = 0.23\kappa$ , and  $\kappa_{\text{int}} = 0.44\kappa$  for device A and  $\kappa/2\pi=0.89$  MHz,  $\kappa_L = 0.32\kappa$ ,  $\kappa_R = 0.59\kappa$ , and  $\kappa_{\text{int}} = 0.09\kappa$  for device B.

A detailed diagram of the laser setup employed in the experiment is shown in Figure S6. A diode-pumped, monolithic non-planar ring oscillator type Nd:YAG laser from Innolight GmbH drives the entire experiment. The laser is first spectrally filtered by passing through a 40 kHz Fabry-Perot optical cavity. Next, the light is doubled passed through an acousto-optical modulator (AOM) used for fast control of the laser frequency. The laser is then split into two components that serve as the signal and meter beams. Each component is passed through another AOM, which provides relative frequency control and independent intensity stabilization of the two beams. The signal beam passes through an in-fiber electro-optical modulator (EOM) that adds frequency sidebands at 18 MHz for Pound-Drever-Hall frequency stabilization of the laser-cavity detuning. At low frequencies the overall optical path length of the cavity is servoed to maintain the cavity resonance with the signal beam. At higher frequencies, up to 100 kHz, the laser frequency is servoed via the common AOM. With this servo system we are able to reduce the cavity-laser frequency fluctuations to the few kilohertz level. The servo output is aggressively filtered to ensure there is no response near  $\omega_m$ . The location of the membrane is passively stable at the few tens of nanometers level during cryogenic operation. To combat drift in the servo lock point, residual amplitude modulation from polarization drift in the EOM is actively canceled. To accomplish this we apply a DC voltage to the EOM crystal to null the amplitude modulation measured by a photodetector sampling the beam after the EOM. With this system, we typically see frequency offset drifts of less than 1 kHz over the tens of minutes times scale relevant to data taking. The signal and meter beams are combined on a polarizing beam splitter, and their polarizations are rotated to match the polarization eigen-axes of the slightly birefringent cavity ( $\sim 400$  kHz birefringence splitting). After the cavity, the two beams are split by another polarizing beam splitter and directed on to individual photodetectors. We typically see less than  $10^{-3}$  cross coupling between the two beams. The photocurrents are simultaneously digitized with a two-channel, 16-bit digital oscilloscope card and a discrete Fourier transformation is applied to the digitized signals to generate power spectra and cross correlations.

The optomechanical system is mounted onto the cold finger of a low-vibration  $^4\text{He}$  flow cryostat from Advanced Research Systems Inc., which attains a base temperature of 4.9 K. The cryostat has windows that allow direct free-space optical access to the cold sample region. We include an additional copper radiation shield with small-aperture, fused-silica windows around our system, heat sunk to the cold finger to ensure our device thermalizes to the cryostat base temperature. In cooling from room temperature to cryogenic temperatures the membrane retains sub-milliradian alignment with the cavity optical axis. We are not inhibited by vibrations from cryogen flow in our system in part due to the low-vibration cryostat design made to eliminate boil off near the cold finger, and in part due to the near-monolithic design of our cavity [24] and high active feedback bandwidth.

## S.2.2 Calibration

The optomechanical coupling of system is calibrated in two ways [24]. Because the signal and meter beams have the same spatial profile, we assume they share a common single-photon optomechanical coupling rate  $g = g_S = g_M$  and coupling constant  $G = gZ_{\text{zp}}$ . At low signal laser power, the effect of the meter beam on the resonator can be predicted by calculations similar to those in the theory section, as is well documented in e.g. Ref. [25]. In the limit where  $\Gamma_0, \Gamma_S \ll \Gamma_M$ , the mechanical damping is given by  $\Gamma_m = \Gamma_M = g^2 N_M \kappa (|\chi_{c2}(\omega_m)|^2 - |\chi_{c2}(-\omega_m)|^2)$ . Using this relation we can extract  $g$  from  $\Gamma_m|_{N_S=0}$  and a measurement of  $N_M = \bar{I}_M / (q_e \epsilon_2 \kappa_R)$  and the cavity parameters. With this method we estimate  $g/2\pi = 15.7$  Hz for device

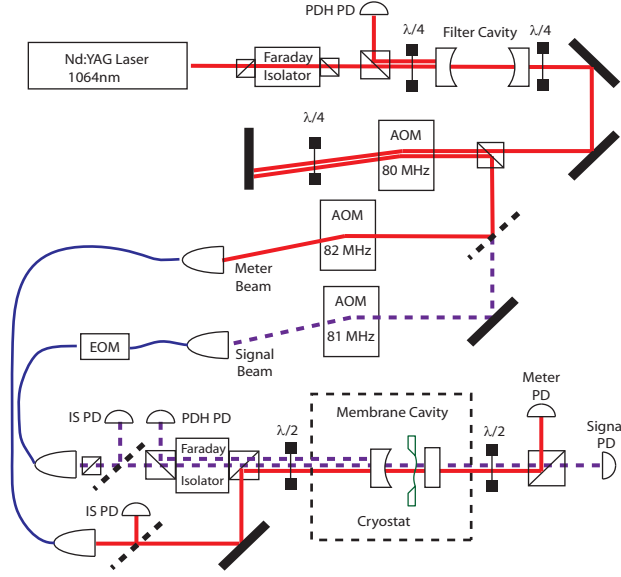


Figure S6: Detailed optical setup. The signal beam (dashed purple) and meter beam (solid red) are derived from a single passively filter 1064 nm source. Acousto-optical modulators (AOM) are used to shift the laser frequency. An electro-optical modulator (EOM) is used to apply frequency sidebands for a Pound-Drever-Hall (PDH) frequency lock. Light is detected at various points using photodetectors (PD). Dashed black lines represent beam splitters, boxes represent polarizing beam splitters.  $\lambda/4$  and  $\lambda/2$  are quarter-wave and half-wave retarders respectively.

A and  $g/2\pi = 16.4$  Hz for device B. Alternatively, we can use the thermal motion of membrane as a known displacement to calibrate  $g$ . The effective temperature of the membrane mode is expected to be given by  $T_{\text{eff}} = T_{\text{bath}}\Gamma_0/\Gamma_m$ . We measure  $T_{\text{bath}}$  from the silicon diode thermometer on the cryostat to be about 4.9 K. Then  $g^2 = (S_{I_M}|_{N_S=0}(\omega_m)/\bar{I}_M^2) \Gamma_m^2 \hbar \omega_m / (8|\Pi_2(\omega_m)|^2 k_b T_{\text{bath}} \Gamma_0)$ , yielding  $g/2\pi = 16.9$  Hz for device A and  $g/2\pi = 15.8$  Hz for device B. For the cross correlation measurements on device B, we measure a slightly smaller mechanical damping rate for the same laser parameters as compared the data in Fig. 1D. Thus we estimate a slightly smaller value of  $g/2\pi = 14.8$  Hz for this data. This difference can be accounted for by a small drift in the membrane position along the optical standing wave gradient between the two measurements.

We estimate the detuning of the signal beam in a variety of ways. For the data of Fig. 1D, we look for linear trends in both  $\Gamma_m$  and the mechanical resonance frequency (the so called “optical spring” effect) as a function of  $N_S$ . Using these trends, we estimate  $\Delta_S/2\pi = 1.5$  kHz for device A and  $\Delta_S/2\pi = 2$  kHz for device B. Alternatively, using the data of Fig. 3A, we fit the cross correlation to the functional form derived above, with  $\Delta_S$  as a free parameter. This fit yields  $\Delta_S/2\pi = 300 \pm 100$  Hz. As mentioned above, the small drift in  $\Delta_S$  over the time between the measurements accounts for the difference in the estimates for device B. Below, in the analysis section, we show how to account for this coherent cooling or heating from the signal laser in order to accurately assess the contribution of RPSN from the mechanical displacement spectrum data. Additionally, as discussed in the theory section, with nonzero  $\Delta_S$ , the cross correlation becomes distorted and contaminated by thermally driven mechanical motion.

The measured classical intensity noise on the signal beam after the cavity is always a small fraction of shot noise. We assess its value and impact on the experiment in several ways. Direct measurements of the total photocurrent power spectrum contain both shot noise and classical noise contributions, as well noise from photodetector dark current. We calibrate the shot noise plus detector noise by illuminating the photodetector with a shot noise limited incandescent light source producing the same average photocurrent as the laser light used in the experiment. We subtract the resulting photocurrent spectrum from  $S_{I_S}(\omega)$  measured during the experiment, and expect the residual to be the classical noise. The recorded shot noise spectral density is within a few percent of the predicted value,  $2q_e I_S$ , based on a careful measurement of the photodetector transimpedance and digitization electronics frequency-dependent gain. However, as the classical noise is typically less than 10% of the shot noise level, this method is subject to significant error. From these measurements we extract a classical noise power spectral density of less than -157 dBc/Hz. We believe the majority of this noise arises from intensity noise imprinted on the laser from the electronics that drive the second AOM on the signal beam path as shown in Figure S6. Because the meter beam passes through an independent AOM with independent electronics, we do not expect any classical noise on the two lasers to be correlated. Thermally occupied mechanical modes of the mirrors and cavity support structure lead to noise in the cavity resonance frequency in the megahertz range. However, because the signal beam is operated close to the cavity resonance, we do not expect a large effect from frequency to amplitude noise conversion by the cavity. We experimentally confirm that we are insensitive to such effects, because our signal beam noise floor is, to good approximation, independent of  $\Delta_S$ .

Classical laser intensity noise can also be detected and differentiated from shot noise by its effects on the membrane mechanics. As pointed out in the theory section above, the phase of the cross correlation spectrum depends on classical versus quantum noise drive. By fitting the phase of  $S_{I_{SM}}(\omega)$ , we estimate that 75% of the correlation signal is due to RPSN, with most of the remainder accounted for by classical radiation pressure noise drive. This value is within the range of the estimate made by direct photodetection of the classical noise. Moreover, by taking into account the measured 25 degree phase shift in the photodetection electronics at frequencies near the mechanical resonance, we find excellent agreement between the absolute phase of the black theoretical curve of Fig. S5(B) and the red measured curve of Fig. 3C.

Another measure of the classical noise level can be extracted from the RPSN data of Fig. 1D (reproduced in Fig. S7). Here, we expect the increase in peak spectral density due to RPSN to scale linearly with the intracavity photon number. However, for a constant classical relative intensity noise, the peak spectral density should scale quadratically with the intracavity photon number. A three term polynomial fit to the data yields a constant term that is related to the thermal motion, a linear term related to RPSN, and a quadratic term related to classical radiation pressure. This method indicates that about 75% of the increase in peak spectral density is due to RPSN in device B for the highest  $N_S$  value employed.

At large circulating optical power, it is possible that absorbed laser light will heat the membrane and increase  $T_{\text{bath}}$ . This effect, in the simplest case, would produce a linear increase in the peak displacement spectral density as function of optical power, the same scaling as RPSN. To control for laser absorption heating, we look at the (4,4) membrane mechanical mode. For the (4,4) mode the optomechanical coupling is weaker, the environmental coupling is stronger and the oscillation frequency higher. Thus we expect only few percent increase in the peak displacement spectral density due to RPSN at the highest drive power. Any significant increase in the amplitude of motion of the (4,4) mode, we may then attribute to spurious heating effects. The data of Figure S7 show the response of the (2,2) and (4,4) mechanical modes for both devices. There is no clear linear trend in either of the (4,4) mode data sets. This allows us to put an upper bound of 10 % for the increase in bath temperature at the largest  $N_S$  employed for both devices, if we assume all of the mechanical modes are coupled to a common thermal bath.

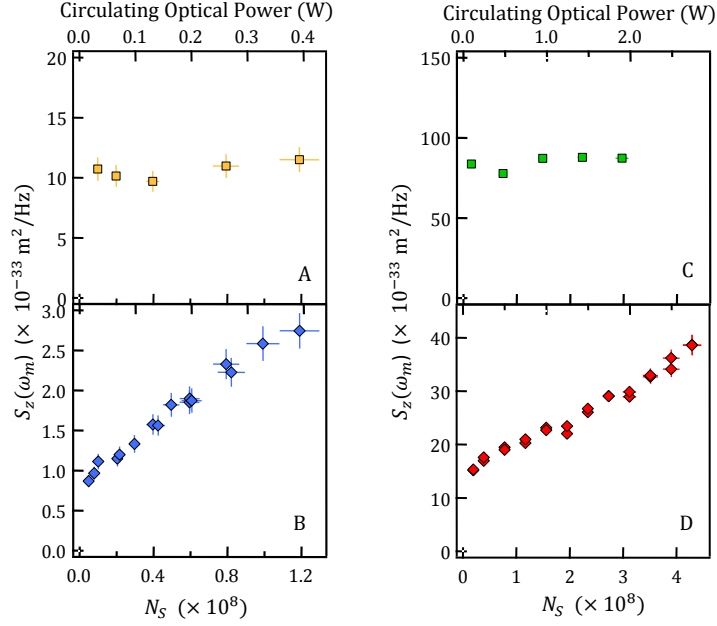


Figure S7: Response of multiple mechanical modes. The peak spectral density is plotted for: part (A) device A (4,4) mode (blue diamonds), part (B) device A (2,2) mode (yellow squares), part (C) device B (4,4) mode (red diamonds), and part (D) device B (2,2) mode (green squares). The (2,2) modes of both devices show a strong linear trend in response to RPSN, while the (4,4) modes show a relatively weak response.

### S.2.3 Data and Analysis

For each point of the device A data in Fig. 1D, we average the power spectra of 1000 records of the photocurrents generated by signal and meter beams. Each record is 20 ms in length and is digitally sampled at  $5 \times 10^7$  samples per second for each laser power setting. We compute  $S_{I_M}(\omega)/\bar{I}_M^2$  and convert this into an effective displacement spectrum using the relation:  $S_z(\omega) = \frac{S_{I_M}(\omega)}{\bar{I}_M^2} \frac{1}{|\Pi_M(\omega)|^2 G^2}$ . Over a region encompassing several mechanical linewidths around the mechanical resonance frequency, we fit each curve to a Lorentzian profile to extract the mechanical linewidth and peak spectral density. For each value of  $N_S$  we record the response of the system for several values of the meter beam power, corresponding to mechanical damping rates ranging from 0.8 to 4 kHz. We perform a linear fit to  $\Gamma_m$  versus  $N_M$  and fit  $S_z(\omega_m)$  inversely proportional to  $N_M$ , to extract an estimate of  $S_z(\omega_m)$  at  $\Gamma_m/2\pi = 3$  kHz.

For the device B data, in Fig. 1D, the signal to noise is much greater, so we only need to average a few hundred records for each laser power. We use only a single meter beam power for each value of  $N_S$ . Again we fit the averaged spectrum to a Lorentzian to extract  $\Gamma_m$  and  $S_z(\omega_m)$ . Because  $\Delta_S$  is a few kilohertz for this data, it provides an additional optomechanical damping and  $\Gamma_m$  shows a linear trend for increasing  $N_S$ , with its value decreasing by about 20 % at the highest signal beam power. By extrapolating to  $N_S = 0$ , we find  $\Gamma_m$  approaches  $2\pi \times 1.43$  kHz in the absence of the signal beam. We then apply a small correction to the  $S_z(\omega)$  data to remove the effect of the optical damping from signal beam.

The dashed theory bounds of Fig. 1B are generated using the calibration methods discussed above. The boundaries are generated by finding the extrema of the theoretical estimate of  $S_z(\omega_m)$  using the two

estimates for  $g$  and the range of estimates for the classical intensity noise contribution. The horizontal error bars on the data represent the systematic uncertainty in the conversion of mean photocurrent to  $N_S$ . The vertical error bars represent statistical error in the measurement.

For the cross correlation data we take 1000 records of 20 ms in length digitally sampled at  $2 \times 10^7$  samples per second. We simultaneously record both photocurrents using a two channel digital oscilloscope card. We use vector averaging to compute the complex cross correlation spectrum, and from the same data also compute the scalar average of the power spectra of the two individual photocurrents. We believe that 1000 averages is sufficient to converge the cross correlation spectrum in region of several mechanical linewidths in spectral width. As evidence, the blue data in Fig. 3B has converged to the same lineshape as the data in Fig. 3A, despite the added mechanical noise. The boundary of the gray theory band of Fig. 3A is again generated as the extrema of the theoretical estimate using estimates for  $g$  and the classical intensity noise level.